Study of a Six-Bed Pressure Swing Adsorption Process

A. Malek and S. Farooq
Dept. of Chemical Engineering, National University of Singapore, 10 Kent Ridge Crescent, Singapore 119260

A mathematical model of a six-bed, ten-step PSA operation is developed. The process cycle considered resembles an industrial hydrogen recovery process from the refinery fuel gas. Three hydrocarbon impurities (methane, ethane, and propane) are considered in the feed gas. The adsorbent used is activated carbon. The nonisothermal, bulk separation PSA model adopts the linear driving force approximation for particle uptake and the extended Langmuir isotherm to represent adsorption equilibrium. A transient pressure equation is incorporated to account for the dynamics in variable pressure steps. The model was verified using experimental results from a computer-controlled, laboratory-scale PSA unit. Considering the complexity of operation, comparison of various stream flow rates, concentrations, bed pressure and temperature profiles indicates that the model provides a sufficiently accurate prediction of the PSA performance. Parametric studies further show that its product purity declines relatively quickly with increasing cycle time and decreasing high operating pressure due to the breakthrough of a relatively sharp methane front. There is no real advantage in operating the PSA unit beyond a high operating pressure of about 18.0 bar.

Introduction

The pressure swing adsorption (PSA) process has undergone significant modifications and improvements over the original design as envisaged by Skarstrom (1960). In that initial design, a two-bed, four-step (pressurization, high-pressure adsorption, blowdown, purge) system was used to dry air. Shortly after the introduction of the Skarstrom process, the Guerin–Domine patent (de Montgareuil and Domine, 1964) demonstrated further potentials of the original Skarstrom cycle. One early modification was the introduction of cocurrent depressurization (Avery and Lee, 1962; Cassidy and Holmes, 1984). This step is beneficial since it helps to increase the concentration of the strongly adsorbed component in the bed voids just prior to the purge step, while still releasing the essentially pure light product remaining near the exit end of the bed. Apart from that, the first major improvement to the PSA process was the introduction of the pressure-equalization step (Marsh et al., 1964; Berlin, 1966; Wagner, 1969). Pressure equalization allows a significant saving in overall process energy consumption since less mechanical energy is required to repressurize the purged, low-pressure bed. Furthermore, product recovery can be increased since less feed/product gas is required to repressurize the bed. The other major improvement to the PSA process was the introduction of multiple beds. Some of the multibed processes, such as those for large-scale production of hydrogen, utilize as much as 10 to 12 beds (Fuderer and Rudelstorfer, 1976). The increased number of beds allows a greater number of pressure-equalization steps, thereby reducing the amount of feed or product gas required for bed repressurization. This results in a tremendous increase in the product recovery, and a further reduction in mechanical-energy consumption at the expense of somewhat higher capital cost. The other advantage is that a more uniform product flow rate can be achieved. Indeed, these two major improvements essentially assured the commercial success of early PSA processes. Other modifications to the PSA process are system-specific, such as the self-purging step in kinetically controlled systems (Knoblauch, 1978) and the use of multiple adsorbents (Fuderer and Rudelstorfer, 1976; Kumar et al., 1992). Sircar (1989) and Jasra et al. (1991) provide a good review of the more important present-day commercial PSA processes.

Correspondence concerning this article should be addressed to S. Farooq.
Present address of A. Malek: Kvaerner R. J. Brown Pte. Ltd., 73 Science Park Drive, Singapore 118254.

There has also been an extensive growth in studies related to the modeling of various PSA processes, as a result of the increasing commercial success of the technology. Reviews on progress in PSA modeling (Yang, 1987; Ruthven et al., 1994) reveal that all the essential features that govern the performance of PSA processes have been progressively addressed in the simulation studies published so far. However, most of these studies are restricted to PSA systems using one type of adsorbent in one or two beds, thus limiting their direct applicability to only a few industrial systems. Notable exceptions, however, are the experimental pilot plant studies of Tomita et al. (1986) and Kumar et al. (1992) on hydrogen purification by PSA that used four-bed and eight-bed processes, respectively. It should be mentioned, though, that detailed mathematical models of these complex processes were not deliberated in the published articles. However, Kumar (1994) provided a mathematical simulation of a four-bed, nine-step PSA process for hydrogen purification where the cyclic operation was approximated by computing the dynamics of a single bed. Transient interbed connectivities were accounted for by using temporal vectors for the relevant stream variables. The study was, however, simplified by considering only a single impurity. Notable among other complex PSA operations that have been recently addressed is a study on air separation for oxygen purification using a four-bed, eight-step cycle (Chou and Huang, 1994; Chiang et al., 1994). The model included the valve equation for depicting dynamic pressure profile, but adopted a local equilibrium (i.e., no particle mass-transfer resistance) model for particle adsorption. This approach can result in an optimistic prediction of separation performance (Chiang et al., 1994). In a more recent work, Chlendi et al. (1995) studied a PSA process involving five components in the feed gas. This work is rather important since, for the first time, two adsorbents were used in a laboratory experimental and theoretical study. However, the PSA unit considered was a two-bed system. Theoretically, multibed PSA systems are more involved than simpler one- or two-bed operations due to the complex interconnectivity of the columns.

Recovery of purified hydrogen from various process gases constitutes the largest commercial application of PSA separation. These processes use 4–12 beds and a combination of different adsorbent types. A complete experimental and modeling study of the more complex commercial operations is yet to be addressed in the open literature. Although the studies with simplified process schemes have established the more important features that govern the separation, the understanding of complex commercial operations using multiple beds, multiple adsorbents, and feed streams with several impurities of variable compositions cannot be derived by simple extrapolation. In fact, extension of the simpler PSA models to develop a reliable model for a complex industrial process is a formidable challenge. Construction and operation of a laboratory-scale PSA unit incorporating all the details of an actual commercial process of significant complexity is equally challenging. Results from such an experimental rig can be used very effectively to verify the simulation model over a wide range of operating conditions. The present study was undertaken to address these challenges.

Experimental studies and modeling of a six-bed PSA process that is similar to that used for the purification of hydrogen from refinery fuel gas is described here. The present study was undertaken as a preamble to a more detailed investigation of an actual industrial multisorbent, six-bed H_2 purification process. In this work, a single-adsorbent process is considered. The adsorbent used is activated carbon and methane, and ethane and propane are the three hydrocarbon impurities considered in the feed. For laboratory experiments, helium is used as the carrier in place of hydrogen as a matter of safety. The equilibrium and kinetic parameters, and their temperature dependence, as well as the bed heat-transfer characteristics are the key input data necessary for the mathematical simulation. These parameters have been established from independent experiments. A simulation model of the six-bed, ten-step PSA operation is developed. The model considers a bulk separation, nonisothermal process, with the linear driving-force model depicting particle uptake and the extended Langmuir isotherm equation representing multicomponent equilibria. A linear pressure differential equation is used to account for the variable pressure steps.

It is shown that the simulation results are in very good agreement with the PSA results obtained using the computer-controlled, experimental unit. In a subsequent work, the model will be extended for studying an actual industrial H_2 purification process.

Theoretical Model

The six-bed PSA process consists of 10 steps comprising the following five operations: high-pressure adsorption, blowdown, purge, product gas repressurization, and pressure equalization. Table 1 shows the cycle sequence. At any time, two beds are producing high-pressure product gas, while one bed is contributing to the vent flow. For the convenience of modeling, a cycle can be viewed as consisting of repetitive blocks of six stages. Each stage can be further divided into three substages. The duration of each stage is the same, and defining the duration of the three substages (t_{c1}, t_{c2}, t_{c3}) is sufficient to define the cycle duration, t_c, since

$$t_c = 6 \times (t_{c1} + t_{c2} + t_{c3}). \quad (1)$$

Figure 1 shows the direction of flow for the various PSA steps. Notably, both pressure-equalization steps are cocurrent flow for the higher pressure beds (cocurrent depressurization). The pressure equalization steps are then followed by a further cocurrent depressurization step where the released gas stream is used to purge another bed. At the end of this step, the bed undergoes countercurrent blowdown, before being purged. The repressurization step is completed using product gas. An additional step (hold) is used to allow for synchronization of the various steps when any of the other step durations is varied.

The theoretical model adopted for the PSA process here is a nonisothermal, bulk-separation model with a nonlinear, multicomponent equilibrium isotherm (the extended Langmuir model). Furthermore, a dynamic model is used for the variable-pressure steps. The model assumptions adopted are summarized below:

1. The flow is represented by an axial-dispersed plug-flow model, with negligible bed pressure drop. Mass dispersion in the axial direction is considered, with negligible radial gradi-

Table 1. Cycle Sequence of Six-Bed PSA Process

	Stage 1	Stage 2	Stage 3	Stage 4	Stage 5	Stage 6
Time (s)	240		35 (t_{c1}) / 50 (t_{c2}) / 35 (t_{c3})	85 / 35	85 / 35	120
Bed 1	**High Pressure Adsorption**		EQ1 / Hold / EQ2	Provide Purge / Blow down	Purge / EQ2	EQ1 + Repressurize
Bed 2	EQ1 + Repressurize	**High Pressure Adsorption**		EQ1 / Hold / EQ2	Provide Purge / Blow down	Purge / EQ2
Bed 3	Purge / EQ2	EQ1 + Repressurize	**High Pressure Adsorption**		EQ1 / Hold / EQ2	Provide Purge / Blow down
Bed 4	Provide Purge / Blow down	Purge / EQ2	EQ1 + Repressurize	**High Pressure Adsorption**		EQ1 / Hold / EQ2
Bed 5	EQ1 / Hold / EQ2	Provide Purge / Blow down	Purge / EQ2	EQ1 + Repressurize	**High Pressure Adsorption**	
Bed 6	**High Pressure Adsorption**	EQ1 / Hold / EQ2	Provide Purge / Blow down	Purge / EQ2	EQ1 + Repressurize	**High Pressure Adsorption**

*EQ. 1 and EQ. 2—pressure equalization steps.

ents. The axial dispersion coefficient was estimated from the correlation of Edwards and Richardson (Ruthven, 1984), as shown in Table 2. Change of flow due to adsorption/desorption, as determined by the overall material balance, is taken into account. The gas is assumed to be ideal.

2. The system is nonisothermal. The column wall and the feed stream are maintained at the same, constant temperature. Thermal dispersion in the axial direction is considered, with negligible radial gradients. Axial thermal conductivity is estimated using the empirical correlation given by Kunii and Smith (1960) and Yagi et al. (1960), as reproduced in Table 2. Heat-transfer resistance in the column is confined to that between the adsorbent bed and the column wall. An experimentally determined, constant effective wall heat-transfer coefficient, h_w, is used to represent heat transfer (Malek and Farooq, 1997). Table 2 shows the magnitude of the heat-transfer coefficient in the column. The gas phase and adsorbent particles are assumed to be in local thermal equilibrium at all times.

3. Three adsorbing components (methane, ethane, and propane) in an inert carrier (helium).

4. The extended Langmuir model is adopted for computing the multicomponent adsorption equilibria. The isotherm parameters had been determined from single-component experiments, with the multicomponent extension verified using multicomponent equilibrium experiments (Malek and Farooq, 1996). The parameters for the adsorption of the three hydrocarbons on activated carbon are given in Table 2. Although the adsorption capacity is considered negligible for the inert carrier (helium), the capacity provided by the particle void for the carrier is taken into account in the material balance.

5. The LDF model is used to represent particle transport. A constant value of the LDF mass-transfer coefficient, calcu-

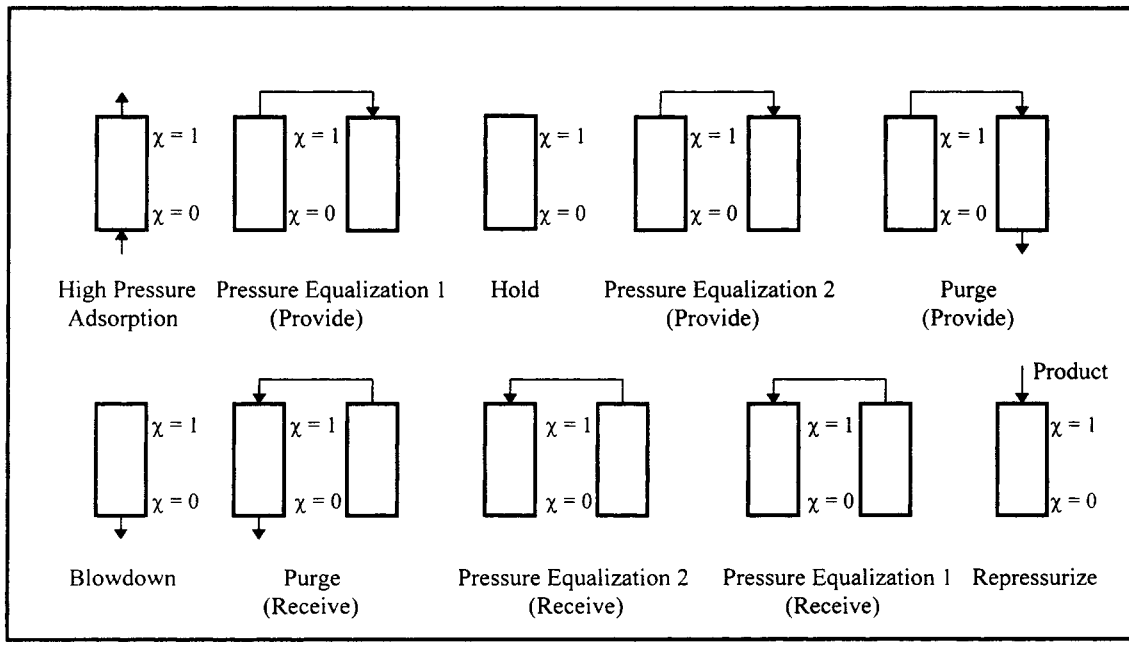

Figure 1. Flow direction for a bed in various steps of the PSA cycle.

Table 2. Equilibrium Parameters and Mass and Wall Heat-Transfer Kinetic Parameters for Adsorption of Hydrocarbons in Activated Carbon*

Hydrocarbon	Langmuir Isotherm Parameters**	$\left[q^* = \frac{q_s^* b_o \exp(-\Delta H_A) P_i}{1 + b_o \exp(-\Delta H_A) P_i}\right]$
Methane	$q_s^* = 5.824 \quad b_o = 1.9178 \times 10^{-4}$	$(-\Delta H_A) = 16.6330 \times 10^3$
Ethane	$q_s^* = 5.474 \quad b_o = 5.6113 \times 10^{-5}$	$(-\Delta H_A) = 25.1015 \times 10^3$
Propane	$q_s^* = 3.735 \quad b_o = 4.1051 \times 10^{-4}$	$(-\Delta H_A) = 26.4418 \times 10^3$

Kinetic parameters†

$$D_{e,\text{ave}} = 0.0085 \qquad h_w = 0.0025$$

Axial Dispersion Parameter

$$\frac{1}{P_{em}} = \frac{g_1 d_p \epsilon_B}{LReSc} + \frac{d_p}{LP_e'\left(1 + \frac{g_1 g_2 \epsilon_B}{ReSc}\right)},$$

where

$$g_1 = 0.73 \qquad g_2 = 13.0 \qquad P_e' = 2.0$$

Axial Thermal Conductivity††

$$K_z = K_{z0} + K_g \delta PrRe$$

$$K_{z0} = K_g\left(\epsilon_B + \frac{1 - \epsilon_B}{\psi + 2/3\,(K_g/K_p)}\right)$$

$$\psi = \psi_2 + (\psi_1 - \psi_2)\left(\frac{\epsilon_B - 0.26}{0.216}\right)$$

where

$$\delta = 0.75 \quad \psi_1 = 0.1 \qquad \psi_2 = 0.07 \quad K_p = 1.0 \times 10^{-2}\ \text{J/cm·s·K}^{\ddagger}$$

*Units are given in the Notation.
**Malek and Farooq (1996).
†Malek and Farooq (1997).
††Gas thermal conductivity, K_g, was estimated using the Eucken formula (Bird et al., 1960). Gas heat capacity and viscosity required for the computation were obtained as functions of temperature from correlations provided in Himmelblau (1996) and Bird et al. (1960), respectively.
‡Estimated from Geankoplis (1993).

lated based on the equilibrium constant at the high-pressure feed conditions, is used as follows

$$k_k = \left(\frac{15\epsilon_p D_{e\,\text{ave}}}{R_p^2}\right)\left(\frac{C_{kf}}{\rho_p q_k^*}\right). \tag{2}$$

In an earlier study (Malek and Farooq, 1997), we showed that it is possible to use an average effective diffusivity, $D_{e,\text{ave}}$ to represent the flux of the three hydrocarbons in the activated carbon particles without significant loss of accuracy. This approach simplifies the kinetic model for hydrocarbon uptake in the particles and is particularly beneficial for multicomponent PSA modeling. The magnitude of the effective diffusivity for the hydrocarbon uptake in activated carbon is shown in Table 2. It is assumed in this study that the mass-transfer kinetics for each adsorbing component is not affected by the presence of the other hydrocarbons in the mixture.

6. The interbed pressure dynamics for the variable pressure steps are estimated using a linear dynamic pressure differential equation as follows:

$$\frac{dP_1}{dt} = -P_c'(P_1 - P_2), \tag{3}$$

where P_1 is the pressure of bed 1 and P_2 is the pressure of bed 2. It should be noted that, in Eq. 3, both P_1 and P_2 are functions of time. In the simulation model, only the pressures of the high-pressure adsorption step, P_H, and the vent, P_L, are required as system inputs. All other intermediate bed pressures are dynamically computed using Eq. 3. For the repressurization step, the column pressure (of bed 1) is computed with the pressure differential given by $(P_1 - P_H)$, while for the blowdown step, the column pressure (of bed 1) is computed with the pressure differential given by $(P_1 - P_L)$.

As essentially similar model of the relevant material and energy-balance equations (for a constant bed pressure) had been used in Malek and Farooq (1997) for single-column breakthrough studies. There, the model was utilized for the determining of the mass- and heat-transfer rate parameters as well as for predicting multicomponent breakthrough behavior. The use of the breakthrough experimental methods in deriving the LDF rate constants ensured that these values are compatible with the PSA model adopted here. Subject to the preceding assumptions, the dimensionless material and thermal-balance equations constituting the PSA simulation model are given below. The derivation of these equations from fundamental material and energy balances is given in the Appendix.

Component material balance:

$$\frac{\partial X_k}{\partial \tau} = \kappa_1 \frac{1}{P_{em}}\left(\frac{\partial^2 X_k}{\partial \chi^2}\right) + \kappa_2 V \frac{\partial X_k}{\partial \chi} + \kappa_3 \sigma X_k\left(1 - \sum_i X_i\right)\frac{1}{\Pi}\frac{d\Pi}{d\tau} - \kappa_3 \sigma X_k \sum_i \frac{\partial X_i}{\partial \tau} - \varphi\left(\frac{dY_k}{d\tau} - X_k \sum_i \gamma_i \frac{dY_i}{d\tau}\right). \tag{4}$$

Boundary conditions:

$$\left.\frac{\partial X_k}{\partial \chi}\right|_{\chi=0} = \kappa_4 \tag{5a}$$

$$\left.\frac{\partial X_k}{\partial \chi}\right|_{\chi=1} = \kappa_5. \tag{5b}$$

Overall material balance:

$$\frac{\partial V}{\partial \chi} = \kappa_6 \frac{1}{P_{em}}\left[\frac{2}{\theta^2}\left(\frac{\partial \theta}{\partial \chi}\right)^2\right] + \kappa_7 \frac{V}{\theta}\frac{\partial \theta}{\partial \chi} + \kappa_8\left[1+\sigma\left(1-\sum_i X_i\right)\right]\frac{1}{\Pi}\frac{d\Pi}{d\tau} - \kappa_8\sigma\sum_i \frac{\partial X_i}{\partial \tau} + \kappa_9\varphi\sum_i \gamma_i \frac{dY_i}{d\tau}. \tag{6}$$

Boundary conditions:

$$V(0,\tau) = \kappa_{10} \tag{7a}$$

$$V(1,\tau) = \kappa_{11}. \tag{7b}$$

Thermal energy balance:

$$\frac{\partial \theta}{\partial \tau} = \kappa_{12}\frac{1}{P_{eh}}\frac{\partial^2 \theta}{\partial \chi^2} + \kappa_{13}\phi_1 V\frac{\partial \theta}{\partial \chi} + \phi_1\varphi\sum_i\left[\gamma_i(\theta+\zeta_i)\frac{dY_i}{d\tau}\right] - \phi_2(\theta-\theta_w). \tag{8}$$

Boundary conditions:

$$\left.\frac{\partial \theta}{\partial \chi}\right|_{\chi=0} = \kappa_{14} \tag{9a}$$

$$\left.\frac{\partial \theta}{\partial \chi}\right|_{\chi=1} = \kappa_{15}. \tag{9b}$$

Column pressure dynamics:

$$\frac{d\Pi_1}{d\tau} = -P_c(\Pi_1 - \Pi_2), \tag{10}$$

where $\Pi_1 > \Pi_2$.

Particle mass-transfer equation (LDF equation):

$$\frac{dY_k}{d\tau} = \alpha_k(Y_k^* - Y_k). \tag{11}$$

Equilibrium isotherm (extended Langmuir):

$$Y_k^* = \frac{\beta_k X_k}{1+\sum_i \beta_i X_i} \tag{12}$$

where

$$\beta_k = b_{ok}\exp\left(\frac{(-\Delta H_A)_k}{RT_f}\frac{1}{\theta}\right)P_f.$$

The initial condition for the PSA simulation model is defined for clean, regenerated beds. In other words, both the gas and solid phases contain no hydrocarbons at the start of the process. This assumption provides the following initial values for the relevant variables:

$$X_k(\chi,0) = 0 \tag{13a}$$

$$Y_k(\chi,0) = 0 \tag{13b}$$

$$\theta(\chi,0) = 1.0. \tag{13c}$$

Because a dynamic bed-pressure equation is used, the initial values of the bed pressures can be simply chosen based on suitable approximations of intermediate pressures between P_H and P_L, which are defined operating parameters, corresponding to the particular step in which each bed starts from. The values of the various step identifiers, κ_i, used before determine the flow and operating configuration for the different steps in the system. These values are shown in Table 3 for the various steps. The constant, P_c, in Eq. (10) for the various variable-pressure steps are also shown in Table 3. Since the nondimensional parameter depends on the feed velocity, a range of values are shown in the table, corresponding to different feed velocity. The appropriate values were determined by fitting the measured pressure profiles.

At this point we discuss the calculations of interstitial velocity and bed pressure for the various steps. In the variable pressure steps, the bed-pressure profile can either be computed using Eq. 10 or using the total balance (Eq. 6). For the pressure-equalization steps, the pressure variation with time for the bed at higher pressure is computed using Eq. 10, with an appropriate value of the coefficient, P_c. The velocity profile in the bed is then calculated using Eq. 6. For the bed at lower pressure, the velocity profile is assumed to vary linearly from the open end to the closed end. The bed-pressure variation with time can then be computed using Eq. 6. The same scheme is used for the purge step, except that in this case, pressure remains constant at the lower pressure bed, and, hence, the velocity profile can be calculated using Eq. 6. For the blowdown and repressurization steps, the pressure changes are calculated using Eq. 10, with the corresponding velocity profiles computed using Eq. 6. The various computation schemes are also indicated in Table 3.

Numerical Solution of PSA Model

A notable feature of the sequence of the six-bed PSA process is the repetitive stages within each cycle. Looking at Table 1, it is clear that there are six distinct stages in a cycle. Each stage is further divided into three substages. The process symmetry allows an efficient way of coding the PSA model, which results in a significant saving of computer memory requirement. The PSA model was solved numerically by using orthogonal collocation to discretize the partial differential equations (Finlayson, 1972; Raghavan and Ruthven,

Table 3. Values of Various Step Identifiers and Constants for the PSA Model

PSA Steps*	κ_1	κ_2	κ_3	κ_4	κ_5	κ_6	κ_7	κ_8	κ_9	κ_{10}	κ_{11}	κ_{12}	κ_{13}	κ_{14}	κ_{15}	P_c
1. HPA	1	−1	0	$-P_{em}V(X_i\|_{\chi=0^-} - X_i\|_{\chi=0^+})$	0	1	1	0	−1	V_f (= 1.0)	Calc.**	1	−1	$-P_{eh}V(\theta\|_{\chi=0^-} - \theta\|_{\chi=0^+})$	0	0
2. PEQ1	1	−1	1	0	0	1	1	−1	−1	0	Calc.**	1	−1	0	0	3.0 to 10.0
3. HD	0	0	0	0	0	0	0	0	−1	0	0	0	0	0	0	0
4. PEQ2	1	−1	1	0	0	1	1	−1	−1	0	Calc.**	1	−1	0	0	3.0 to 10.0
5. PPG	1	−1	1	0	0	1	1	−1	−1	0	Calc.**	1	−1	0	0	2.5 to 8.0
6. BD	1	1	1	0	0	1	1	1	1	Calc.**	0	1	1	0	0	3.0 to 10.0
7. RPG	1	1	0	0	$P_{em}V(X_i\|_{\chi=1^+} - X_i\|_{\chi=1^-})$	1	1	0	1	Calc.**	$V_1\Pi_1/\Pi_2$	1	1	0	$P_{em}V(\theta\|_{\chi=1^+} - \theta\|_{\chi=1^-})$	0
8. REQ2	1	1	1	0	$P_{em}V(X_i\|_{\chi=1^+} - X_i\|_{\chi=1^-})$	1	1	1	1	0	$V_1\Pi_1/\Pi_2$	1	1	0	$P_{em}V(\theta\|_{\chi=1^+} - \theta\|_{\chi=1^-})$	Pres. calc.†
9. REQ1	1	1	1	0	$P_{em}V(X_i\|_{\chi=1^+} - X_i\|_{\chi=1^-})$	1	1	1	1	0	$V_1\Pi_1/\Pi_2$	1	1	0	$P_{em}V(\theta\|_{\chi=1^+} - \theta\|_{\chi=1^-})$	Pres. calc.†
10. RPR	1	1	1	0	$P_{em}V(X_i\|_{\chi=1^+} - X_i\|_{\chi=1^-})$	1	1	1	1	0	Calc.**	1	1	0	$P_{em}V(\theta\|_{\chi=1^+} - \theta\|_{\chi=1^-})$	2.0 to 6.0

*HPA—High-pressure adsorption; PEQ1—provide pressure equalization 1; HD—hold; PEQ2—provide pressure equalization 2; PPG—Provide purge; BD—blowdown; RPG—receive purge; REQ2—receive pressure equalization 2; REQ1—receive pressure equalization 1; RPR—repressurize.
**Velocity profile calculated from total material balance.
†Bed pressure calculated from total material balance assuming a linear velocity profile in bed.

1983). The Appendix includes a brief description of the solution of the PSA model using orthogonal collocation. The discretization is done for the spatial variable, resulting in a set of ODEs in the time domain. A 19-point collocation was found to be a suitable compromise between minimizing the magnitude of oscillations in the solution of the derivative equations and the overall computation time. The set of ODEs are rather stiff, and were solved using an implicit backward differentiation formula (Brown et al., 1989). The overall material balance equation was converted to a set of linear algebraic equations and was solved using LU-decomposition. Figure 2 shows a flow chart of the sequence followed in solving the PSA simulation model. At each step, the relevant process equations were solved iteratively for each bed using the parameter values and solution methods detailed in Tables 2 and 3. At the end of each step, the final conditions of gas- and solid-phase variables in each bed were stored and used as the initial conditions for the next phase. The model was coded in FORTRAN and solved on a Cray J916 supercomputer. The Parallel Vector Processor computer runs at a cycle speed of 100 MHz. Generally, solution of the nonisothermal, multicomponent, six-bed PSA process required about 700 CPU seconds per cycle and more than 16 Mbyte of main memory.

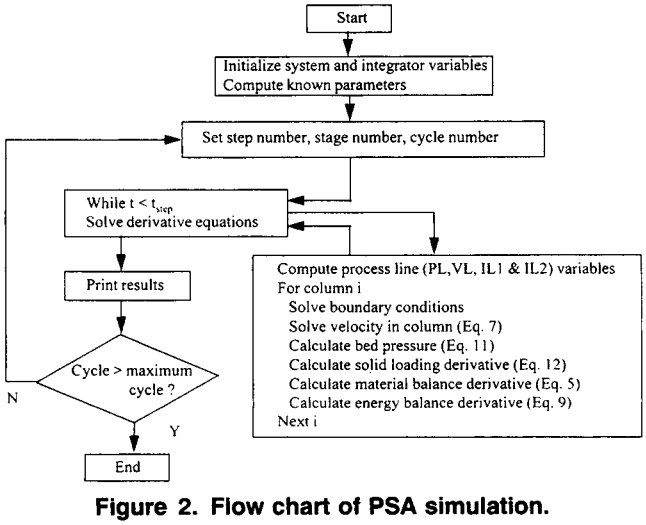

Figure 2. Flow chart of PSA simulation.

Experimental PSA Unit

A laboratory version of the actual industrial six-bed pressure-swing adsorption unit was constructed for elaborate experimental studies. The system mainly consisted of six jacketed, stainless-steel columns containing activated carbon adsorbents. Water from a temperature-regulated tank was circulated through the jacket using a magnetic, centrifugal pump. Table 4 shows some relevant data on the columns and ad-

Table 4. PSA Experimental Information

Column:	*Jacketed stainless steel*
Internal diameter:	4.0 cm
Length:	40.0 cm
Adsorbent:	*Activated carbon*
Apparent density*:	0.87 g·cm^{-3}
Particle porosity**:	0.58
Mean pore radius**:	18×10^{-8} (18 Å)
Specific surface area**:	970 m^2·g^{-1}
Particle heat capacity†:	0.95 J/g·K
Particle size:	2.36–2.80 mm (Tyler equiv. 8-mesh and 7-mesh)
Bed void fraction:	0.38
Adsorbate:	Mixture of methane, ethane, and propane (no other contaminants)
Carrier:	Helium
Experimental range:	
Interstitial gas velocity	0.427 to 0.715 cm/s
Cycle time	600 to 840 s
Pressure	P_H = 9.8 bar; P_L = 2.8 bar
Temperature	299.15 K

*Apparent density of adsorbent was provided by the manufacturer.
**Experimentally measured in this laboratory. Mean pore radius and specific surface area were determined using mercury porosimetry.
†Approximated based on values given in Table 3-205 in Perry's *Chemical Engineers' Handbook*, 6th ed., McGraw-Hill, New York, 1984.

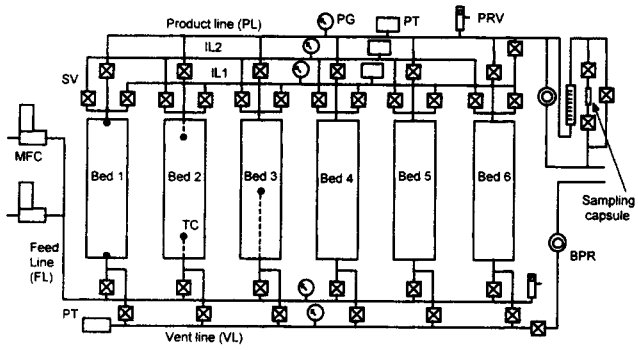

Figure 3. Experimental 6-bed PSA unit.

Legend: BPR—back-pressure regulator; MFC—mass-flow controller; PG—pressure gauge; SV—solenoid valve; PRV—pressure-relief valve; PT—pressure transducer; TC—thermocouple.

sorbent used, while Figure 3 shows the experimental setup. The six columns were interconnected through five main pipelines, namely, the feed line (FL), the product line (PL), the vent line (VL), and two intermediate lines (IL1 and IL2). Line PL was maintained at the highest process pressure, P_H, and line VL was maintained at the lowest process pressure, P_L, using GO BP3 back-pressure regulators. The two intermediate lines were used for connecting the beds during the pressure-equalization steps. Each column was also directly connected to five accompanying dc-operated Honeywell Skinner ON/OFF solenoid valves. These valves were used to configure the flow path into and out of the columns at each time step in the cyclic process. With regard to process flow sequence, at any time, two beds were fed with high-pressure feed using line FL. Similarly, the high-pressure products from the two beds were mixed in line PL. Depending on the exact cycle stage, line VL was either carrying the exiting gas from a purged bed or blowdown gas. Line IL1 was used for the first level of pressure equalization (Pressure Equalization 1), as well as for repressurization with product gas, while IL2 was used for the second-level pressure equalization (Pressure Equalization 2) and for the purge step.

The highly automated experimental setup also included two pressure-compensating feed-flow controllers, four pressure transducers, and one flowmeter. The feed-flow controllers used were Brooks Model 5850E (0–10 L/min. for the carrier) and Model 5850TR (0–2 L/min. for the hydrocarbons). The laboratory-calibrated mass-flow controllers provided an accuracy of about $\pm 1.0\%$ of full scale (including the control/readout device accuracy). The product and vent flow rates were determined using a rotary, wet-gas meter. Lines PL, IL1, and IL2 were fitted with E&H Cerabar pressure transducers, while line VL was fitted with a TransInstrument pressure transducer. These calibrated transducers afforded an accuracy of approximately $\pm 2.0\%$. All the transducers used were dc-operated and provided an analog output signal of 0–5 V. In addition, five K-type thermocouples were fitted, radially centered, into three of the six beds at various depths in order to measure the transient temperature profile in the bed. Each thermocouple was housed in a 1/8 in. stainless-steel tube packed with hardened magnesium oxide and sealed at both ends. These allow leak-proof, high-temperature measurements. The accuracy of the thermocouples is approximately ± 0.25°C. Gas samples were taken from both product and vent lines for analysis on a Perkin Elmer Autosystem GC fitted with a TCD and a Supelco Carboxen-1004 Micropacked Column. The gas samples were collected using a small tube fitted with leak-proof, Swagelok Quick Connect fittings.

Data acquisition and valve-sequencing control were performed using a dedicated personal computer running on an Intel Pentium 75 MHz CPU. A 12-bit A/D card was used to directly read the signals from the flow and pressure transduc-

Table 5. Operating Conditions of Single-sorbent PSA Experimental and Simulation Runs*

Run No.	P_H (bar)	P_L (bar)	v_f (cm/s)	$X_{f1}/X_{f2}/X_{f3}$	$t_{c1}/t_{c2}/t_{c3}$
			Experimental		
PAC1	9.8	2.8	0.427	0.177/0.065/0.03	35/50/35
PAC2	9.8	2.8	0.573	0.176/0.065/0.03	35/50/35
PAC3	9.8	2.8	0.715	0.170/0.065/0.02	35/50/35
PAC4	9.8	2.8	0.573	0.179/0.068/0.02	35/30/35
PAC5	9.8	2.8	0.573	0.177/0.064/0.03	35/70/35
			Numerical Simulation		
SAC1	9.8	2.8	0.427	0.177/0.065/0.03	35/50/35
SAC2	9.8	2.8	0.573	0.176/0.065/0.03	35/50/35
SAC3	9.8	2.8	0.715	0.170/0.065/0.02	35/50/35
SAC4	9.8	2.8	0.573	0.179/0.068/0.02	35/30.35
SAC5	9.8	2.8	0.573	0.177/0.064/0.03	35/70/35
SAC6	9.8	2.8	0.427	0.177/0.065/0.03	35/30/35
SAC7	9.8	2.8	0.427	0.177/0.065/0.03	35/70/35
SAC8	9.8	2.8	0.427	0.177/0.065/0.03	35/90/35
SAC9	14.0	2.8	0.427	0.177/0.065/0.03	35/50/35
SAC10	16.0	2.8	0.427	0.177/0.065/0.03	35/50/35
SAC11	18.0	2.8	0.427	0.177/0.065/0.03	35/50/35
SAC12	22.0	2.8	0.427	0.177/0.065/0.03	35/50/35
SAC13	18.0	2.8	0.427	0.177/0.065/0.03	35/30/35
SAC14	18.0	2.8	0.427	0.177/0.065/0.03	35/70/35
SAC15	18.0	2.8	0.427	0.177/0.065/0.03	35/90/35
SAC16	18.0	2.8	0.573	0.177/0.065/0.03	35/50/35

*All runs conducted with feed and column wall temperature of 299.15 K.

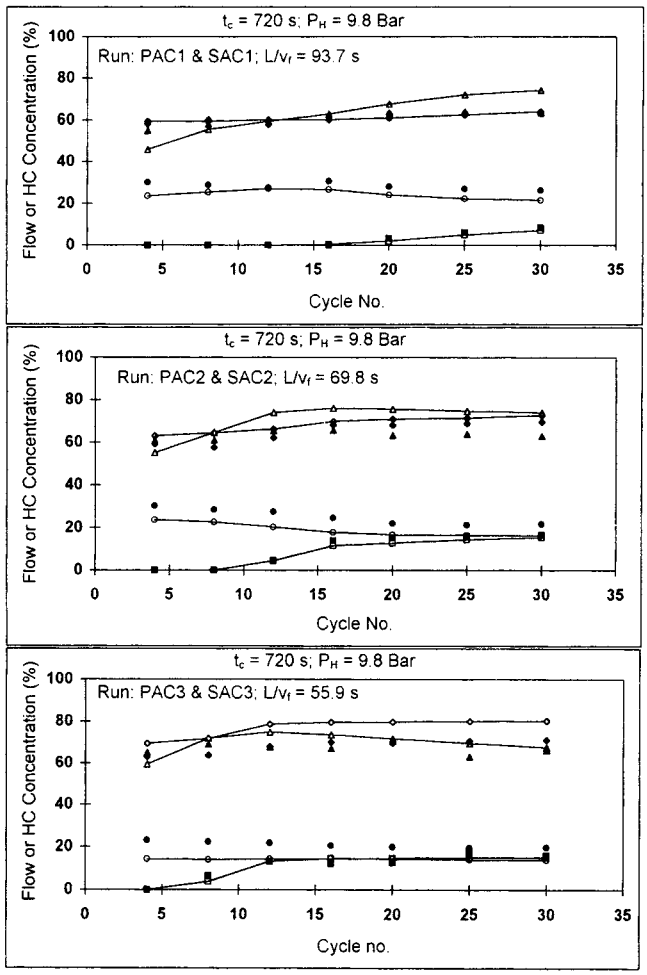

Figure 4. Effect of L/v_f ratio on PSA performance.

■—product concentration; ♦—product flow; ▲—vent concentration; ●—vent flow; lines with open symbols are corresponding simulation results; operating conditions are given in Table 5.

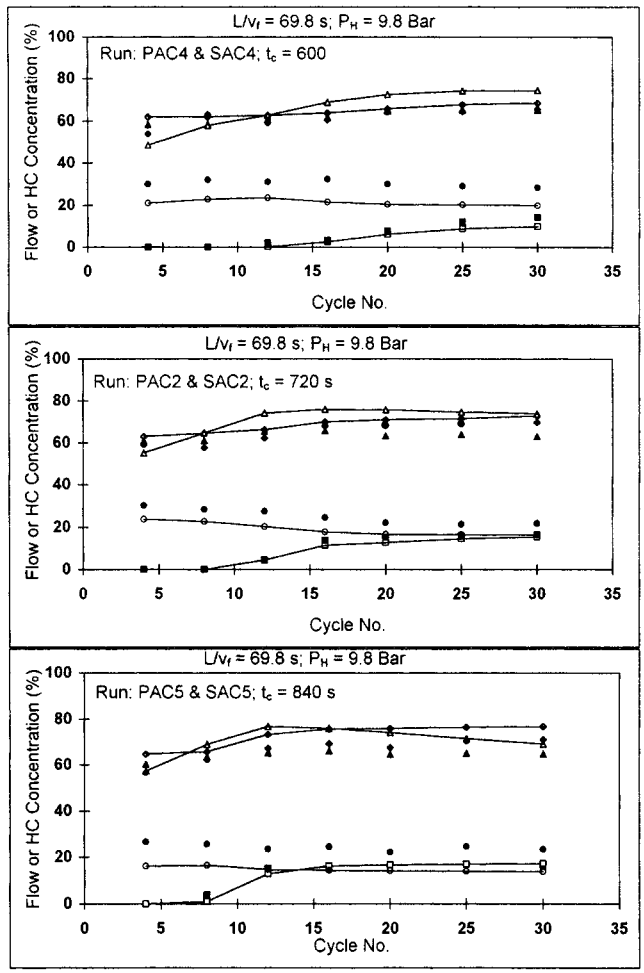

Figure 5. Effect of cycle time, t_c, on PSA performance.

■—product concentration; ♦—product flow; ▲—vent concentration; ●—vent flow; lines with open symbols are corresponding simulation results; operating conditions are given in Table 5.

ers. Thermocouple signals were measured using another 12-bit A/D card (PC-LabCard Model 818), connected to an amplifier/multiplexer daughter card with cold-junction compensation (PC-LabCard Model 789). The 32 solenoid valves were controlled using two 24-bit digital I/O card (PC-LabCard Model 724), each connected to a 24-channel, Form C power-relay output board (PC-LabCard Model 7225). For this purpose, the Form C relay switch is particularly beneficial, since each channel can then be used either in the normal open (NO) or normal closed (NC) mode, thereby allowing the desired flexibility in configuring the flow path in the six-bed process. The entire data-acquisition/control system implemented was software programmable. In this regard, an integrated, real-time, Windows-based process interface was custom-designed and coded using event-driven Microsoft Visual Basic. This provided a convenient means of operating the experimental setup.

Experimental and Simulation Results

In this section, the effectiveness of the simulation model in predicting the experimental PSA results is investigated. The verified model is then used for further process studies. The main parameters studied experimentally are the effects of feed velocity and cycle time on the separation behavior, as well as the pressure and temperature dynamics. Table 5 summarizes the operating conditions adopted for the various experimental and simulation runs conducted. It is pertinent to mention here that the operating conditions of the experimental (as well as simulation) runs had been judiciously chosen to allow for significant breakthrough of at least one hydrocarbon component. This is to provide a more reliable comparative study between the experimental and simulation results, since the flow and concentration parameters are more direct performance indicators of a PSA unit. Temperature and pressure measured in the beds served as additional data sources for model verification.

In all the experimental runs, the feed hydrocarbon compositions were nearly constant. Similarly, the highest and lowest bed pressures, P_H and P_L, respectively, were maintained constant during the experimental runs using back-pressure regulators. Premixed bottled gas was used as feed, and the available supply arrangement allowed the experimental runs to be continued up to 30 cycles. However, as is shown later,

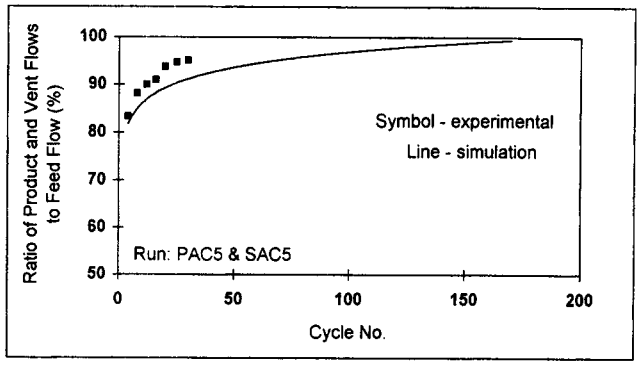

Figure 6. Material balance of a PSA run.

Operating conditions are given in Table 5.

many more cycles are required in order to achieve cyclic steady state for this PSA process. All the simulation runs were thus continued for a large number of cycles in order to provide a better understanding of the process dynamics. The product and vent flow rates used in the analysis are shown as percentages of feed flow to the PSA unit, while concentrations of these two streams are shown as the total hydrocarbon mole percent in the respective streams. The flow and concentration results from the product line were obtained at the end of the high-pressure adsorption step. For the vent line, the results were obtained during the purge step.

Figures 4 and 5 show the flow and concentration results from the experimental and corresponding simulation runs conducted. Referring to Figure 4, increasing feed velocity, v_f, increases product recovery and decreases vent flow as a percentage of feed flow. There is also an earlier breakthrough of methane in the product stream, as well as a higher concentration of hydrocarbons in the vent stream. These observations are consistent since a higher feed flow to the PSA unit results in increasing hydrocarbon content in the PSA beds. Moreover, increasing the duration of the high-pressure adsorption step has a similar effect on the flow rates and concentrations, as shown in Figure 5. Discernibly, the simulation model is capable of accurately predicting both product concentration and flow for the various feed flow rates and cycle times. Although the model underpredicts the vent flow rate and overpredicts the vent concentration, the quantitative difference is not very large and the variations in the vent flow and concentration with number of cycles are correctly predicted.

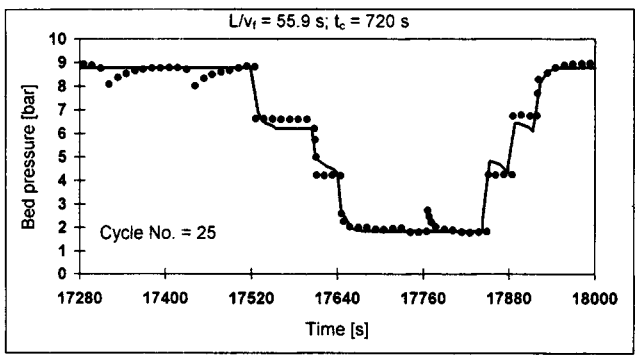

Figure 7. Comparison of experimental and simulated pressure–time history in the bed.

Symbols—experimental (PAC3); Line—simulation (SAC3); operating conditions are given in Table 5.

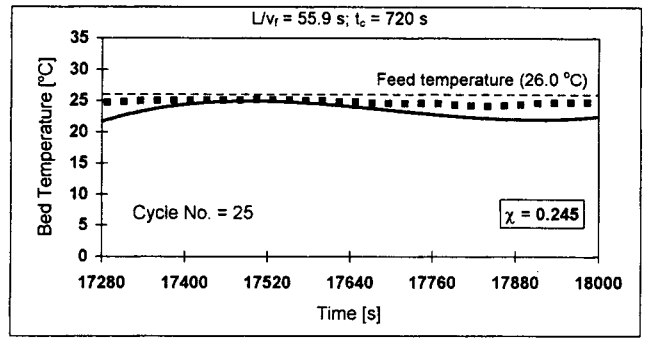

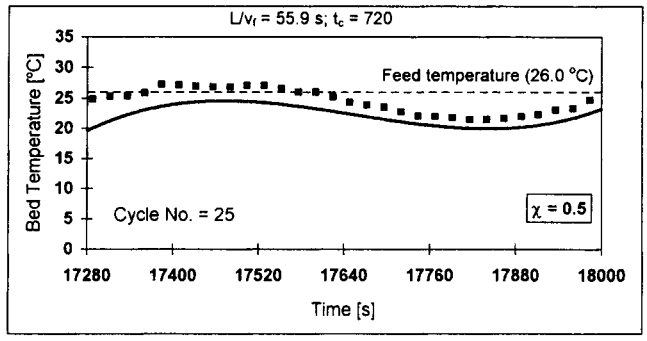

Figure 8. Comparison of experimental and simulated temperature–time history at two different locations in the bed.

Symbols—experimental (PAC3); line—simulation (SAC3); operating conditions are given in Table 5.

As a further analysis, Figure 6 shows a typical material balance obtainable from the simulation model as compared with actual experimentally measured flow rates for one of the runs. The plot shows the ratio of the cumulative exit flow rate from the PSA unit (i.e., flow in the product and vent lines) to the feed stream entering the unit. The simulation suggests that over 150 cycles are required for achieving true steady state under this operating condition. However, a somewhat faster approach to cyclic steady state is indicated by the experimentally observed trend.

In the experiments conducted, both pressure and temperature changes in the bed were measured continuously with time. This allowed a direct comparison between the experimental and simulated pressure and temperature history for each cycle as a function of time. Figure 7 shows a representative pressure profile measured experimentally as well as that obtained from the simulation model. In the simulation model, and high system pressure, P_H, and vent pressure, P_L, are given as inputs, while all other intermediate pressures are computed dynamically. This condition parallels the actual experimental run, where both P_H and P_L are controlled using back-pressure regulators, with the intermediate pressures being dynamically dictated by the conditions in the interconnected beds. Figure 7 shows that the computed pressure–time history is generally comparable with that measured experimentally. With regard to the bed temperature–time history

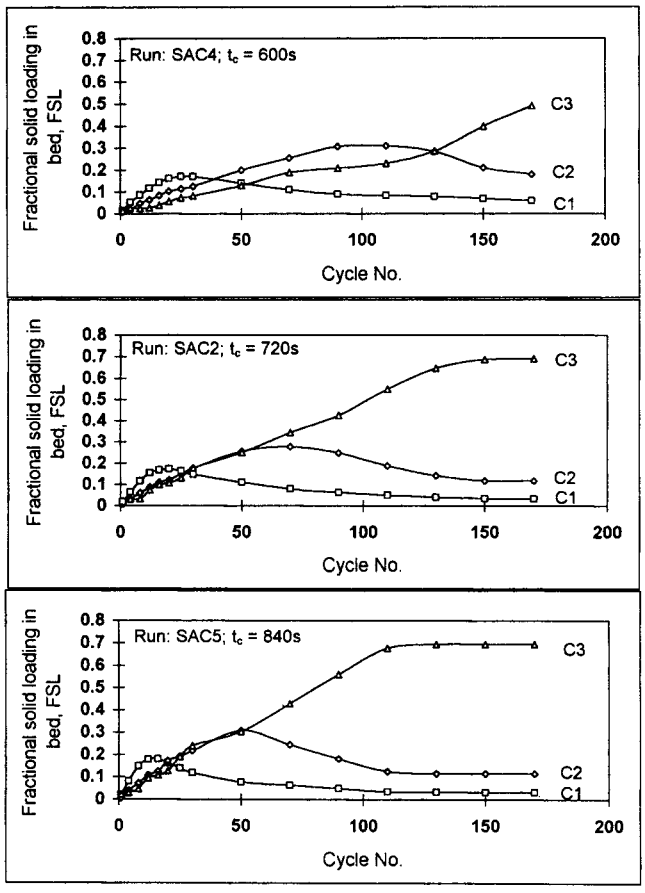

Figure 9. Approach of the bed solid loading to cyclic steady state.

C1—methane; C2—ethane; C3—propane; operating conditions are given in Table 5.

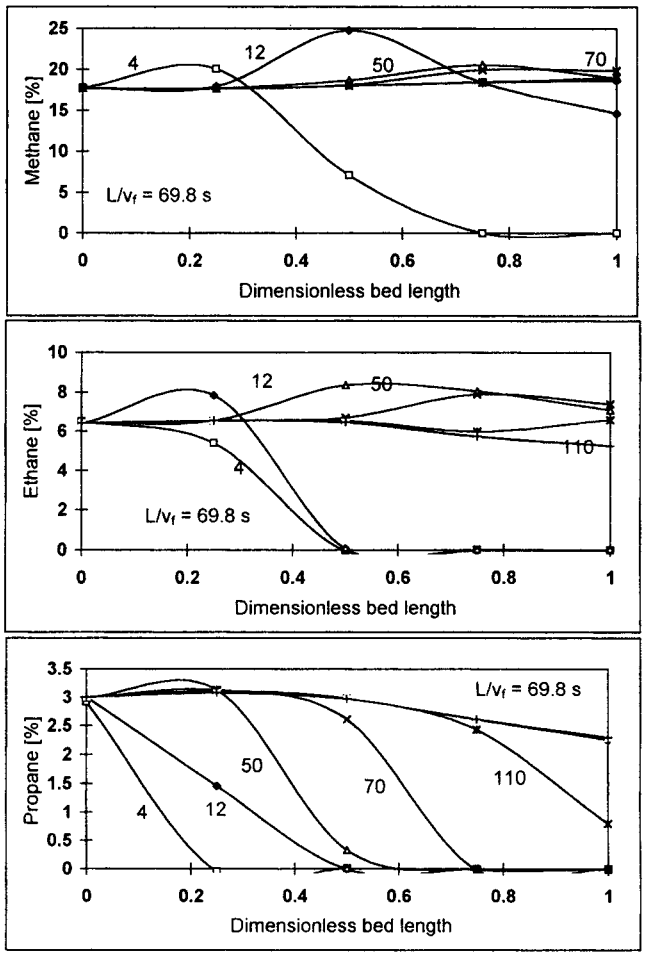

Figure 10. Gas-phase concentration profiles as a function of cycle number.

Run—SAC5; P_H = 9.8 bar; other operating conditions are given in Table 5.

in the bed, Figure 8 shows a comparison between the experimentally measured and simulated results for the same run. The general trends in the temperature–time history at different points in the bed are also correctly predicted. Thus, from this comparative study, it is apparent that the simulation model can predict the sorbate flux, temperature, and pressure dynamics of the actual PSA process reasonably well.

Having verified the adequacy of the simulation model developed here, we then used it extensively to better understand the system dynamics. The additional simulation results follow. As mentioned earlier, all the simulation runs were conducted up to very large cycle numbers in order to study the approach of the system dynamics to cyclic steady state. Figure 9 shows the fractional solid loading (FSL) for each adsorbable component as a function of the cycle number at three different cycle times. The fractional solid loading for component k, FSL_k, is defined as follows:

$$FSL_k = \int_0^1 \frac{q_k^*}{q_{sk}^*} d\chi. \tag{14}$$

For long cycle times, cyclic steady state is reached earlier. Cyclic steady state for the methane component is nearly independent of the cycle time, since there is significant breakthrough of that component for all the cycle times considered here. The corresponding transient gas-phase concentration profiles of the adsorbable components along the bed length for run SAC5, showing the approach to steady state, are given in Figure 10. The numbers in the figure indicate the cycle number. As expected, there is an observable dependence between the gas-phase and the solid-phase concentration dynamics. In particular, for the run considered, the methane component reaches cyclic steady state in less than 50 cycles, the ethane component in about 100 cycles, and the propane component in about 120 cycles. Although very little separation is achievable at the low operating-pressure ratio (P_H/P_L) employed for this run, the results are important for a clearer understanding of the bed dynamics. The variation of the bed temperature profile with cycle number is also of interest. Figure 11a shows the bed temperature profiles at various cycle number at the end of the high-pressure adsorption step, while Figure 11b shows the profiles at the end of the purge step. In contrast to the concentration profiles in the bed, the movement of the transient temperature profile is relatively slow and apparently reaches cyclic steady state after about 12 cycles in this case. Hence, monitoring the concentration breakthrough by temperature sensing is likely to be misleading.

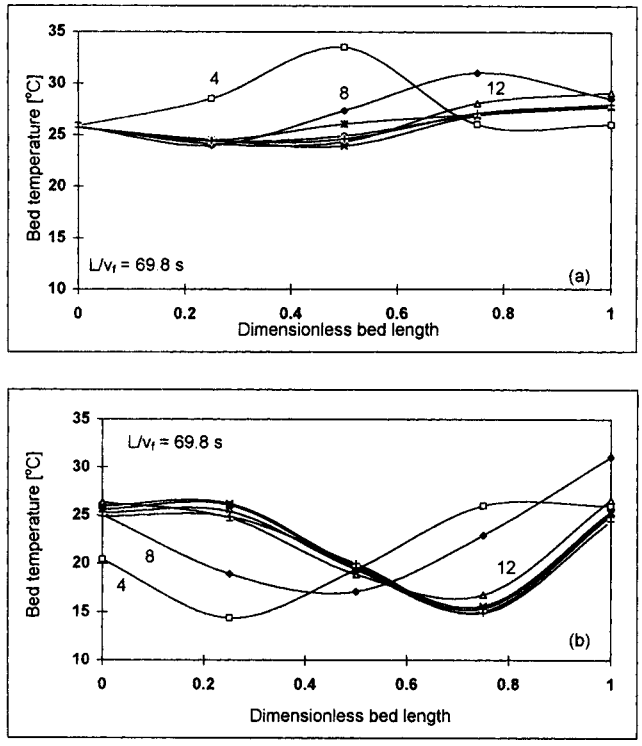

Figure 11. Variation of bed axial temperature profiles with cycle number.

(a) At the end of the high-pressure adsorption step. (b) At the end of the purge step. Run—SAC5; operating conditions are given in Table 5.

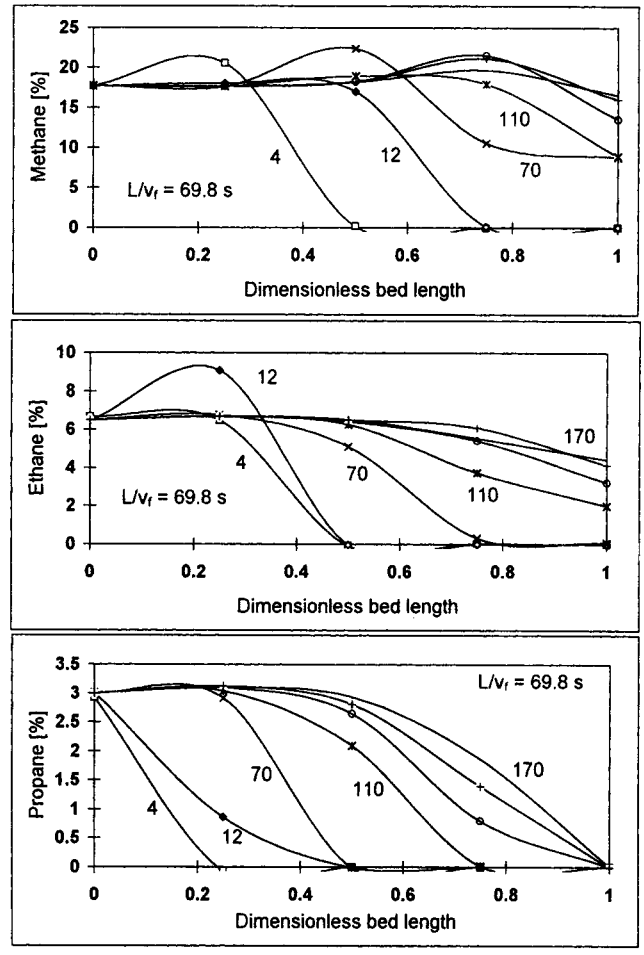

Figure 12. Gas-phase concentration profiles as a function of cycle number.

Run—SAC16; P_H = 18.0 bar; other operating conditions are given in Table 5.

The effect of increasing the operating pressure ratio on the cyclic steady state is shown in Figure 12. The figure shows the results of transient gas-phase concentrations in the bed for a P_H of 18.0 bar (cf. Figure 10, where P_H = 9.8 bar). Approach to cyclic steady state is slightly delayed under this condition.

The effects of cycle time on product recovery and purity are shown in Figure 13. Figure 13a shows the recovery and purity obtainable for a P_H of 9.8 bar. In this case, the recovery increases monotonically with cycle time, t_c, while the purity decreases monotonically. For a higher operating pressure of 18.0 bar, Figure 13b shows that a high product purity can be achieved at low cycle time at the expense of a lower product recovery. However, the purity drops quickly at longer cycle times due to the breakthrough of methane, which forms the largest fraction of hydrocarbon. Hence, it is clear that the favorable operating conditions for the PSA process are high adsorption pressure and short cycle time.

With regard to the effect of system pressure on the operations, Figure 14 shows a plot of the product recovery and product purity obtainable using the single-sorbent, six-bed PSA process as a function of the high operating pressure, P_H. The figure indicates a gradual increase in the product purity with the operating pressure, which levels off at P_H greater than 18.0 bar. At a low operating pressure ratio, there is complete breakthrough of methane and ethane, as well as a significant amount of propane. At a higher adsorption pressure, there is only partial breakthrough of methane and ethane, with almost complete retention of propane at cyclic steady state. The product recovery, on the other hand, decreases with operating pressure and then levels off after a P_H of about 16.0 bar. Considering the variation in both recovery and purity, as well as the expected increase in operating cost with increasing system pressure, it is apparent that there is no significant advantage in operating the PSA unit at a pressure higher than 18.0 bar.

As mentioned earlier, hydrocarbon transport in activated carbon particles considered in this study is through Knudsen and surface diffusion. This was determined experimentally using the breakthrough method up to a column pressure of about 6 bar (Malek and Farooq, 1996). Although molecular diffusion is inversely proportional to pressure, we have calculated that even at a high operating pressure (~ 20 bar) used in the PSA study, the molecular diffusivity is about two orders of magnitude larger than both the Knudsen and surface diffusivities. Hence, mass transport in the particles is still essentially controlled by the latter two diffusion mechanisms.

Conclusions

A mathematical model of a 6-bed, 10-step PSA process has been developed. The cycle configuration used resembles that

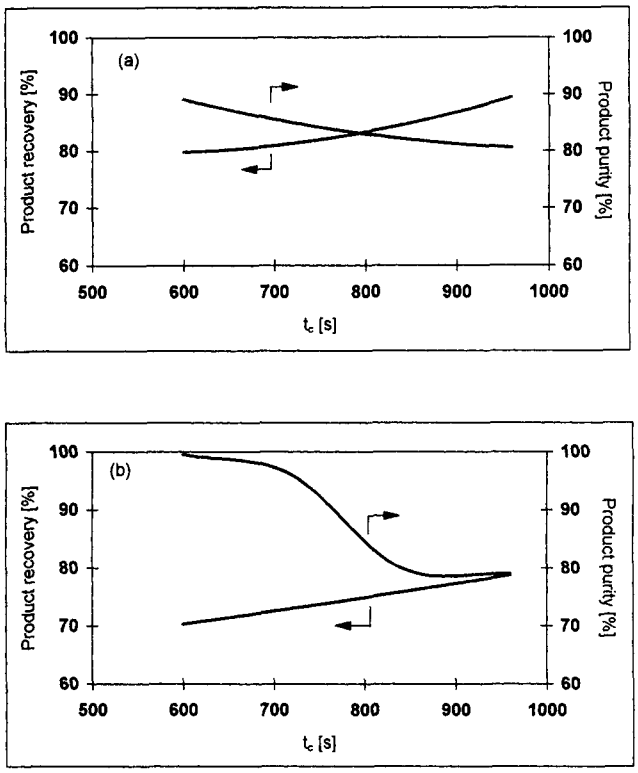

Figure 13. Product recovery and purity as a function of cycle time.

(a) For $P_H = 9.8$ bar (runs SAC1, SAC6, SAC7, and SAC8). (b) For $P_H = 18.0$ bar (runs SAC11, SAC13, SAC14, and SAC15). Other operating conditions are given in Table 5.

of hydrogen purification from refinery fuel gas. A laboratory-scale, computer-controlled, six-bed PSA rig has also been constructed and made operational to exactly reproduce the industrial cycle. The performance of the numerical model has been examined with experimental results from the laboratory unit using activated carbon adsorbent, and with methane, ethane, and propane as contaminants. The comparisons indicate that the product concentration and flow rates are well predicted by the model. Given the complexity of operation, the quantitative agreement is excellent. Furthermore, the variations in these parameters with number of cycle are correctly predicted. The variations of the pressure and temperature profiles in the bed are also well predicted.

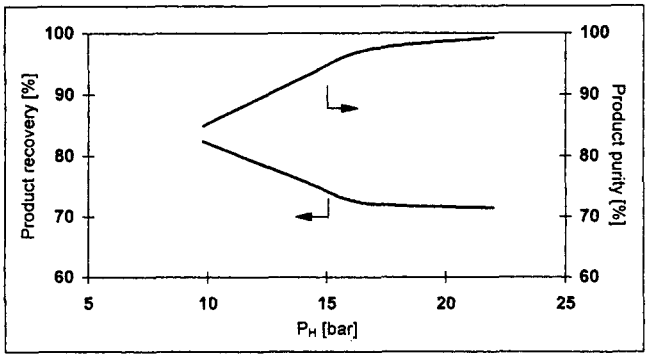

Figure 14. Product recovery and purity obtainable using the single-sorbent, 6-bed PSA process as a function of the high operating pressure, P_H.

Runs SAC1, SAC6, SAC7, and SAC8; $t_c = 720$ s; other operating conditions are given in Table 5.

Parametric studies of the process using the mathematical model show that more than 100 cycles are required to reach cyclic steady state. Interestingly, however, the bed temperature profile seems to attain steady state much quicker, after about 15 cycles. Further simulations show that, for this system, the product purity declines relatively quickly with increasing cycle time and decreasing high operating pressure. This is basically due to the sharp breakthrough of the methane front. There is, however, no real advantage in operating the PSA unit beyond a high operating pressure of about 18.0 bar, since the subsequent improvement in product purity is only marginal.

In this study, hydrogen, which is expectedly weakly adsorbed on activated carbon, has been replaced by helium as carrier in the experiments for safety reasons. Moreover, refinery fuel gas also normally contains trace amounts of higher molecular-weight hydrocarbons as well as moisture in addition to the three light hydrocarbons considered here. The problem of addional contaminants is generally tackled by using multiple adsorbents in order to improve the overall separation performance. These remaining deficiencies in the six-bed process model developed here will be addressed in our next communication.

Notation

b_o = equilibrium isotherm model parameters, bar
C = component concentration in the gas phase, mol/cm^3
C_T = total concentration in the gas phase, mol/cm^3
(C_p) = heat capacity, J/g·K
d_p = mean particle diameter, cm^2/s
D_e = effective diffusivity in particle, cm^2/s
D_L = axial dispersion, cm^2/s
D_m = molecular diffusivity, cm^2/s
$e = (1 - \epsilon_B)/\epsilon_B$
g_1, g_2 = constants in computing axial dispersion parameter (Table 2)
K_p = particle thermal conductivity, J/cm·s·K
K_z = effective-bed thermal conductivity, J/cm·s·K
L = column length, cm
P_c' = coefficient in the interbed pressure-dynamic equation (Eq. 3)
$P_c = (P_c' L)/v_f$
$P_{eh} = \{\epsilon_B v_f L[C_T(C_p)_g + e\rho_p(C_p)_s]\}/K_z$, heat Peclet number
$P'_{eh} = [v_f L C_T(C_p)_g]/K_z$, heat Peclet number for boundary condition
$P_{em} = v_f L/D_L$, mass Peclet number
$Pr = [(C_p)_g \mu]/K_g$, Prandtl number
q = adsorbed phase concentration, mmol/g·m
q^* = equilibrium adsorbed-phase concentration, mmol/g·m
R = universal gas constant (= 8.314 J/mol·K)
Re = Reynolds number, $(\rho_g v_f \epsilon_B d_p)/\mu$
R_i = column internal-wall radius, cm
R_p = mean particle radius, cm
Sc = Schmidt number, $\mu D_m/\rho_g$
$t_{c1/2}$ = PSA half cycle time, s
T = temperature, K
$V = v/v_f$, dimensionless velocity
X = adsorbate mole fraction in gas phase
$Y = q/q_s^*$, dimensionless solid-phase concentration
$Y^* = q^*/q_s^*$, dimensionless equilibrium solid-phase concentration
z = space dimension, cm

Greek letters

$\alpha = Lk/v_f$
$\beta_k = b_{ok}\exp\{[(-\Delta H_A)_k/(1/RT_f)](1/\theta)\}P_f$
$\chi = z/L$, dimensionless axial distance
δ = constant in computing axial thermal conductivity (Table 2)
ϵ = void fraction
$\phi_1 = [C_T(C_p)_g]/\{C_T(C_p)_g + e\rho_p(C_p)_s\}$
$\phi_2 = (2h_w L)/[R_i v_f \epsilon_B C_T(C_p)_g + e\rho_p(C_p)_s]$
$\gamma_i = q^*_{si}/q^*_{s1}$
$\varphi = e\rho_p(q^*_{s1}/C_T)$
$\Pi = P/P_H$, dimensionless pressure
μ = viscosity
$\theta = T/T_f$, dimensionless temperature
ρ = particle density
$\sigma = e\epsilon_p$
ψ_1, ψ_2 = constants in computing axial thermal conductivity (Table 2)
$\tau = v_f t/L$, dimensionless time
$\zeta = (-\Delta H_A)/[(C_p)_g T_f]$
$(C_p)_g$ = gas heat capacity, J/g·K
$(C_p)_s$ = particle heat capacity, J/g·K
$(-\Delta H_A)$ = heat of adsorption, J/mol

Subscripts

1,2,3 = methane, ethane, and propane, respectively
a = adsorbate
B = adsorbent
f = inlet conditions
g = gas phase
i,k = adsorbate components in multicomponent adsorption
I = inert
m,n = collocation points
p = particle
w = column wall

Literature Cited

Avery, W. F., and M. N. Y. Lee, "ISOSIV Process Goes Commercial," *Oil Gas J.*, 121 (June, 1962).

Berlin, N. H., "Method for Providing an Oxygen-Enriched Environment," U.S. Patent No. 3,280,536 (1996).

Bird, R. B., W. E. Stewart, and E. N. Lightfoot, *Transport Phenomena*, Wiley, New York (1960).

Brown, P. N., G. D. Byrne, and A. C. Hindmarsh, "VODE: A Variable Coefficient ODE Solver," *SIAM J. Sci. Stat. Comput.*, **10**, 1038 (1989).

Cassidy, R. T., and E. S. Holmes, "Twenty-Five Years of Progress in Adiabatic Adsorption Processes," *AIChE Symp. Ser.*, **80**(233), 68 (1994).

Chiang, A. S. T., Y. L. Chung, C. W. Chen, T. H. Hung, and T. Y. Lee, "Experimental Study on a Four-bed PSA Air Separation Process," *AIChE J.*, **40**, 1976 (1994).

Chlendi, M., D. Tondeur, and F. Rolland, "A Method to Obtain a Compact Representation of Process Performances from a Numerical Simulator: Example of Pressure Swing Adsorption for Pure Hydrogen Production," *Gas Sep. Purif.*, **9**, 125 (1995).

Chou, C. T., and W. C. Huang, "Simulation of a Four-bed Pressure Swing Adsorption Process for Oxygen Enrichment," *Ind. Eng. Chem. Res.*, **33**, 1250 (1994).

de Montgareuil, P. G., and D. Domine, "Process for Separating a Binary Gaseous Mixture by Adsorption," U.S. Patent No. 3,155,468 (1964).

Finlayson, B. A., *The Method of Weighted Residuals and Variational Principles*, Academic Press, New York (1972).

Fuderer, A., and E. Rudelstorfer, "Selective Adsorption Process," U.S. Patent No. 3,846,849 (1976).

Geankoplis, C. J., *Transport Processes and Unit Operations*, 3rd ed., Prentice-Hall, Englewood Cliffs, NJ (1993).

Himmelblau, D. M., *Basic Principles and Calculations in Chemical Engineering*, 6th Ed., Prentice Hall, Englewood Cliffs, NJ (1996).

Jasra, R. V., N. V. Choudary, and S. G. T. Bhat, "Separation of Gases by Pressure Swing Adsorption," *Sep. Sci. Tech.*, **26**(7), 885 (1991).

Knoblauch, K., "Pressure Swing Adsorption: Geared for Small Volume Users," *Chem. Eng.*, **85**(25), 87 (1978).

Kumar, R., W. C. Kratz, D. E. Guro, D. L. Rarig, and W. P. Schmidt, "Gas Mixture Fractionation to Produce Two High Purity Products by Pressure Swing Adsorption," *Sep. Sci. Tech.*, **27**(4), 509 (1992).

Kumar, R., "Pressure Swing Adsorption Process: Performance Optimum and Adsorbent Selection," *Ind. Eng. Chem. Res.*, **33**, 1600 (1994).

Kunii, D., and J. M. Smith, "Heat Transfer Characteristics in Porous Rocks," *AIChE J.*, **6**, 71 (1960).

Malek, A., "A Study of Hydrocarbon Purification from the Refinery Fuel Gas By Pressure Swing Adsorption," PhD Thesis, Dept. of Chemical Engineering, National Univ. of Singapore (1996).

Malek, A., and S. Farooq, "Kinetics of Hydrocarbon Adsorption on Activated Carbon and Silica Gel," *AIChE J.*, **43**(3), 761 (1997).

Malek, A., and S. Farooq, "Comparison of Isotherm Models for Hydrocarbon Adsorption on Activated Carbon," *AIChE J.*, **42**(11), 3191 (1996).

Marsh, W. D., F. S. Pramuk, R. C. Hoke, and C. W. Skarstrom, "Pressure Equalization Depressurizing in Heatless Adsorption," U.S. Patent No. 3,142,547 (1964).

Raghavan, N. S., and D. M. Ruthven, "Numerical Simulation of a Fixed Bed Adsorption Column by the Method of Orthogonal Collocation," *AIChE J.*, **29**(6), 922 (1983).

Ruthven, D. M., *Principles of Adsorption and Adsorption Processes*, Wiley, New York (1984).

Ruthven, D. M., S. Farooq, and K. S. Knaebel, *Pressure Swing Adsorption*, VCH Publishers, New York (1994).

Sirkar, S., "Pressure Swing Adsorption Technology," *Adsorption: Science and Technology*, A. E. Rodrigues, M. D. Levan, and D. Tondeur, eds., NATO ASI Series E158, Kluwer Academic Publishers, Dordrecht, The Netherlands, p. 285 (1989).

Skarstrom, C. W., "Method and Apparatus for Fractionating Gaseous Mixtures by Adsorption," U.S. Patent No. 2,944,627 (1960).

Tomita, T., T. Sakamoto, U. Ohkama, and M. Suzuki, *The Effects of Variables in Four-bed Pressure Swing Adsorption*, I. L. Athanasios, ed., Engineering Foundation, New York (1986).

Wagner, J. L., "Selective Adsorption Process," U.S. Patent No. 3,430,418 (1969).

Yagi, S., D. Kunii, and N. Wakao, "Studies on Axial Effective Thermal Conductivities in Packed Beds," *AIChE J.*, **6**(4), 543 (1960).

Yang, R. T., *Gas Separation by Adsorption Processes*, Butterworth, Boston (1987).

Appendix: Solution of the PSA Model Using Orthogonal Collocation

The derivation of the PSA model is as follows. For a multicomponent, nonisothermal, nonisobaric process, the component material balances in the adsorption bed for sorbate and inert are given by

$$-\frac{\partial C_k}{\partial t} = -D_L\frac{\partial^2 C_k}{\partial z^2} + \frac{\partial v C_k}{\partial z} + \frac{1-\epsilon_B}{\epsilon_B}\rho_p\frac{dq_k}{dt} \quad \text{(A1)}$$

$$-\left(1+\frac{1-\epsilon_B}{\epsilon_B}\epsilon_p\right)\frac{\partial C_I}{\partial t} = -D_L\frac{\partial^2 C_I}{\partial z^2} + \frac{\partial v C_I}{\partial z}. \quad \text{(A2)}$$

It should be noted that sorbate adsorption capacity, q^*_k, includes the capacity in the adsorbent particle void. In contrast, the inert carrier balance includes only the capacity provided by the particle void, since the adsorbent has no significant adsorptive capacity for the carrier. Assuming ideal-gas law holds, expansion of Eq. A1 results in the following nondimensional form:

$$\frac{\partial X_k}{\partial \tau} = \frac{1}{P_{em}}\left(\frac{\partial^2 X_k}{\partial \chi^2} - \frac{2}{\theta}\frac{\partial X_k}{\partial \chi}\frac{\partial \theta}{\partial \chi} + \frac{2X_k}{\theta^2}\left(\frac{\partial \theta}{\partial \chi}\right)^2 - \frac{X_k}{\theta}\frac{\partial^2 \theta}{\partial \chi^2}\right) - \left(V\frac{\partial X_k}{\partial \chi} + X_k\frac{dV}{d\chi} - \frac{VX_k\partial\theta}{\theta\partial\chi}\right) - \frac{X_k}{\Pi}\frac{\partial \Pi}{\partial \tau} + \frac{X_k}{\theta}\frac{\partial \theta}{\partial \tau} - \varphi\gamma_k\frac{dY_k}{d\tau}. \quad \text{(A3)}$$

Axial pressure gradient has been neglected in the derivation of Eq. A3 in conformance with the model assumptions adopted in this study. Summing the component material balance equations provide the following overall material balance equation in dimensionless form:

$$\frac{dV}{d\chi} = \frac{1}{P_{em}}\left(\frac{2}{\theta^2}\left(\frac{\partial \theta}{\partial \chi}\right)^2 - \frac{1}{\theta}\frac{\partial^2 \theta}{\partial \chi_2}\right) + \frac{V}{\theta}\frac{\partial \theta}{\partial \chi} - \left[1+\sigma\left(1-\sum_i \frac{\partial X_i}{\partial \tau}\right)\right]\frac{1}{\Pi}\frac{d\Pi}{d\tau} + \left[1+\sigma\left(1-\sum_i \frac{\partial X_i}{\partial \tau}\right)\right]\frac{1}{\theta} \times \frac{\partial \theta}{\partial \tau} - \varphi\sum_i \gamma_i\frac{dY_i}{d\tau} + \sigma\sum_i \frac{\partial X_i}{\partial \tau}. \quad \text{(A4)}$$

Some of the higher order terms in Eq. A4 are negligible due to their small magnitudes (Malek, 1996). Without significant loss of accuracy, the following simplified form of the equation can be used:

$$\frac{dV}{d\chi} = \frac{1}{P_{em}}\frac{2}{\theta^2}\left(\frac{\partial \theta}{\partial \chi}\right)^2 + \frac{V}{\theta}\frac{\partial \theta}{\partial \chi} - \left[1+\sigma\left(1-\sum_i \frac{\partial X_i}{\partial \tau}\right)\right]\frac{1}{\Pi}\frac{d\Pi}{d\tau} - \varphi\sum_i \gamma_i\frac{dY_i}{d\tau} + \sigma\sum_i \frac{\partial X_i}{\partial \tau}. \quad \text{(A5)}$$

Substituting Eq. A5 into Eq. A3 and ignoring inconsequential terms results in the following simplified form of the component material balance equation:

$$\frac{\partial X_k}{\partial \tau} = \frac{1}{P_{em}}\frac{\partial^2 X_k}{\partial \chi^2} - V\frac{\partial X_k}{\partial \chi} + \sigma\left(1-\sum_i \frac{\partial X_i}{\partial \tau}\right)\frac{X_k}{\Pi}\frac{d\Pi}{d\tau} - \varphi\left(\gamma_k\frac{dY_k}{d\tau} - X_k\sum_i \gamma_i\frac{dY_i}{d\tau}\right) - \sigma X_k\sum_i \frac{\partial X_i}{\partial \tau}. \quad \text{(A6)}$$

An energy balance for the system, with axial thermal conduction and constant wall temperature, yields

$$(1-\epsilon_B)\rho_p(C_p)_s\frac{\partial T}{\partial t} = K_z\frac{\partial^2 T}{\partial z^2} - \epsilon_B C_T T(C_p)_g \frac{dv}{dz} - \epsilon_{BT}(C_p)_g\frac{T}{P}\frac{dP}{dt} + (1-\epsilon_B)\rho_p(-\Delta H_A)\sum_i \times \frac{dq_i}{dt} - \frac{2h_w}{R_B}(T-T_w). \quad \text{(A7)}$$

Substituting for the velocity gradient from Eq. A5 and ignoring inconsequential terms results in the following nondimensional form:

$$\frac{\partial \theta}{\partial \tau} = \frac{1}{P_{eh}}\frac{\partial^2 \theta}{\partial \chi^2} - \phi_1 V\frac{\partial \theta}{\partial \chi} + \phi_1\varphi\sum_i \left(\gamma_i(\theta+\zeta_i)\frac{dY_i}{d\tau}\right) - \phi_2(\theta-\theta_w). \quad \text{(A8)}$$

The Danckwerts boundary conditions are applicable for the concentration and temperature derivative equations as follows:

$$\left.\frac{\partial X_k}{\partial \chi}\right|_{\chi=0} = -P_{em}V_f(X_{kf}-X_k) \quad \text{(A9a)}$$

$$\left.\frac{\partial X_k}{\partial \chi}\right|_{\chi=1} = 0 \quad \text{(A9b)}$$

$$\left.\frac{\partial \theta}{\partial \chi}\right|_{\chi=0} = -P'_{eh}V_f(\theta_f-\theta) \quad \text{(A9c)}$$

$$\left.\frac{\partial \theta}{\partial \chi}\right|_{\chi=1} = 0. \quad \text{(A9d)}$$

In the solution scheme adopted in this study, the PDEs depicting the component material and energy balances (Eqs. A6 and A8) are discretized in the spatial dimension to generate a set of time-derivative ODEs. The discretization is done using orthogonal collocation. In this way, $(M+2)$, or $M2$, points are chosen within the spatial dimension, with $\chi(1)$ and $\chi(M2)$ indicating the two boundary points. In using orthogonal collocation, the first- and second-order spatial derivatives of the concentration and temperature variables are replaced by the equivalent summation terms involving the $\boldsymbol{A}$ and $\boldsymbol{B}$ matrices (Finlayson, 1972). The collocation points can be chosen as the roots of a Legendre-type polynomial. In the present study, roots of the orthogonal Jacobi polynomial have been used to generate the collocation points (Malek, 1996).

Discretization of the gas- and solid-phase concentrations as well as the temperature variable results in a set of M first-order time-derivative equations as follows:

$$\frac{dX_k(m)}{d\tau} = \frac{1}{P_{em}}\sum_{n=1}^{M2} B(m,n)X_k(n) - V(m)\sum_{n=1}^{M2} A(m,n)X_k(n) + \sigma\left(1-\sum_i \frac{dX_i(m)}{d\tau}\right)\frac{X_k(m)}{\Pi}\frac{d\Pi}{d\tau} - \varphi\left(\gamma_k\frac{dY_k(m)}{d\tau} - X_k(m)\sum_i \gamma_i\frac{dY_i(m)}{d\tau}\right) - \sigma X_k(m)\sum_i \frac{dX_i(m)}{d\tau} \quad \text{(A10)}$$

$$\frac{d\theta(m)}{d\tau} = \frac{1}{P_{eh}}\sum_{n=1}^{M2} B(m,n)\theta(i) - \phi_1 V(m)\sum_{n=1}^{M2} A(m,n)\theta(n) + \phi_1\varphi\sum_i \left(\gamma_i(\theta(m)+\zeta_i)\frac{dY_i(m)}{d\tau}\right) - \phi_2(\theta(m)+\theta_w), \quad \text{(A11)}$$

where $m = 2, 3, \ldots, M1$ and $n = 1, 2, \ldots, M2$.

Discretization of the boundary conditions gives the following equations:

$$\sum_{n=1}^{M2} A(1,n)X_k(n) = -P_{em}V_f[X_{fk} - X_k(1)] \quad \text{(A12a)}$$

$$\sum_{n=1}^{M2} A(M2,n)X_k(n) = 0 \quad \text{(A12b)}$$

$$\sum_{n=1}^{M2} A(1,n)\theta(n) = -P'_{eh}V_f[\theta_f - \theta(1)] \quad \text{(A12c)}$$

$$\sum_{n=1}^{M2} A(M2,n)\theta(n) = 0. \quad \text{(A12d)}$$

The boundary variables for the concentration and temperature can be solved separately from the other internal points by proper algebraic manipulation of Eqs. A12.

The overall material balance equation (Eq. A5) is also discretized in the same manner giving the following:

$$\sum_{n=1}^{M2} A(m,n)V(n) = \frac{1}{P_{em}}\frac{2}{\theta(m)^2}\left(\sum_{n=1}^{M2} A(m,n)\theta(n)\right)^2 + \frac{V(m)}{\theta(m)}\sum_{n=1}^{M2} A(m,n)\theta(n) - \left[1+\sigma\left(1-\sum_i \frac{dX_i(m)}{d\tau}\right)\right]\frac{1}{\Pi}\frac{d\Pi}{d\tau} - \varphi\sum_i \gamma_i \frac{dY_i(m)}{d\tau} + \sigma\sum_i \frac{dX_i(m)}{d\tau}, \quad \text{(A13)}$$

where $m = 1, 2, \ldots, M2$. Discernibly, a set of algebraic equations results that can be conveniently solved using a linear equation solver such as LU decomposition.

Equations A10 to A13 are the collocation forms of the model equations. The set of ODEs and algebraic equations thus derived were then solved (solution procedure is outlined in the main text) to obtain the dependent variables as functions of time and position in the column.

Manuscript received Feb. 3, 1997, and revision received June 5, 1997.